Environ Fluid Mech (2010) 10:587–602
DOI 10.1007/s10652-009-9165-0

ORIGINAL ARTICLE

# Large Eddy Simulation of turbulence generated by a weak breaking tidal bore

**Pierre Lubin · Hubert Chanson · Stéphane Glockner**

Received: 16 September 2009 / Accepted: 21 December 2009 / Published online: 13 January 2010


**Abstract** A tidal bore is a natural and fragile phenomenon, which is of great importance for the ecology of an estuary. The bore development is closely linked with the tidal range and the river mouth shape, and its existence is sensitive to any small change in boundary conditions. Despite their ecological and cultural value, little is known on the flow field, turbulent mixing and sediment motion beneath tidal bores. Indeed, some striking features can be highlighted in two-dimensional simulations, such as large velocity fluctuations and flow recirculation structures. Using Large Eddy Simulation method, the numerical results emphasised the complicated turbulent structures and their unsteadiness under a tidal bore.

**Keywords** Environmental flows · Navier-Stokes equations · Large Eddy Simulation · Tidal bores

## 1 Introduction

A tidal bore is a positive surge propagating upstream as the tidal flow turns to rising in river mouths exhibiting converging funnelled channel forms during low freshwater conditions. The flow of the river sometimes flows upstream after its passage. It is a fascinating, intense and powerful natural phenomenon (Fig. 1), attracting many people to watch it or even surf it in many locations [3]. The tidal bores impact significantly the river mouths and estuarine systems. The turbulent mixing and dispersion are enhanced by the bore, because some

**Electronic supplementary material** The online version of this article (doi:10.1007/s10652-009-9165-0) contains supplementary material, which is available to authorized users.

P. Lubin (✉) · S. Glockner
TREFLE-ENSCBP UMR 8508 CNRS, Université de Bordeaux, 16 Avenue Pey-Berland,
33607 Pessac Cedex, France
e-mail: lubin@enscbp.fr

H. Chanson
School of Civil Engineering, The University of Queensland, Brisbane, QLD 4072, Australia

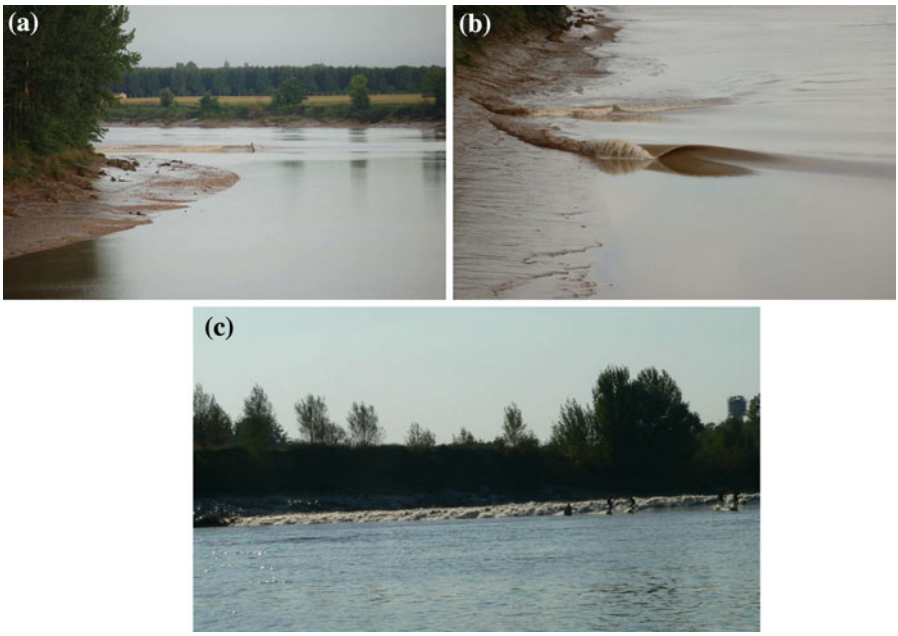


**Fig. 1** Tidal bore of the Garonne river (France). The river flows towards the background of the pictures, whereas the tidal flow propagates towards the foreground of the pictures. **a** Surfer riding the bore front. **b** First wave breaking on the left bank (Langoiran—France). **c** Weak breaking bore (Podensac—France)

significant bed erosion and scour take place beneath the bore while suspended material are advected upstream with the tidal bore [4]. However, a tidal bore is a delicate process and it results from a fragile balance between many parameters (e.g. bathymetry, tidal conditions, etc.) [6]. For example, some dredging and river training yielded the disappearance of several tidal bores. To date, very few field observations were conducted [26,28–31] often with some limited spatial and temporal resolution, while some recent laboratory experiments brought new insights to the turbulent motion [2,13–15]. Nevertheless, the tidal bore processes remain poorly understood today [4]. A recent numerical model based upon the Navier-Stokes equations [8] was compared to laboratory experiments [13]. Some interesting features were observed, but the results lacked a fine mesh grid resolution and accurate numerical schemes.

The goal of the present work is to simulate this unsteady two-phase tidal bore motion using a Large Eddy Simulation (LES) method to gain a further understanding of the tidal bore processes. The numerical data are compared with some detailed laboratory data and the results are discussed. We aim at describing accurately the free-surface behavior and the turbulent flow structure.

## 2 Numerical model and validation

### 2.1 Mathematical formulation

An incompressible multiphase phase flow between non-miscible fluids can be described by the Navier-Stokes equations in their multiphase form. In the single fluid formulation of the

problem [12], a phase function $C$, or "color" function, is used to locate the different fluids standing $C = 0$ in the outer medium, $C = 1$ in the considered medium. The interface between two media is repaired by the discontinuity of $C$ between 0 and 1. In practice, $C = 0.5$ is used to characterize this surface. The governing equations for the Large Eddy Simulation (LES) of an incompressible fluid flow are classically derived by applying a convolution filter to the unsteady Navier-Stokes equations. The resulting set of equations describes the entire hydrodynamics and geometrical processes involved in the motion of multiphase media (Eqs. 1–3):

$$\nabla \cdot \mathbf{u} = 0 \tag{1}$$

$$\rho \left( \frac{\partial \mathbf{u}}{\partial t} + \mathbf{u} \cdot \nabla \mathbf{u} \right) = -\nabla p + \rho \mathbf{g} + \nabla \cdot (\mu + \mu_t) \left[ \nabla \mathbf{u} + \nabla^T \mathbf{u} \right] \tag{2}$$

and

$$\frac{\partial C}{\partial t} + \mathbf{u} \cdot \nabla C = 0 \tag{3}$$

where $\mathbf{u}$ is the velocity, $C$ the phase function, $t$ the time, $p$ the pressure, $\mathbf{g}$ the gravity vector, $\rho$ the density, $\mu$ the dynamic viscosity and $\mu_t$ the turbulent viscosity. The magnitude of the physical characteristics of the fluids depends on the local phase. They are defined according to $C$ in a continuous manner as:

$$\begin{aligned} \rho &= C\rho_1 + (1 - C)\rho_0 \\ \mu &= C\mu_1 + (1 - C)\mu_0 \end{aligned} \tag{4}$$

where $\rho_0$, $\rho_1$, $\mu_0$ and $\mu_1$ are the densities and viscosities of fluid 0 and 1 respectively. The turbulent viscosity $\mu_t$ is calculated with the Mixed Scale model [24], which has proved its accuracy for coastal applications [10,20].

### 2.2 Discretization and solvers for the momentum equations

The time discretization is implicit and the equations are discretized on a staggered grid thanks to the finite volume method. A dual grid, or underlying grid [23], is used to gain an improved accuracy for the interface description, the mesh grid size being divided by two in each direction for the interface tracking. This technique also allows to avoid the interpolations of the physical characteristics on the staggered grids, since the color function is defined on each point where viscosities and densities are needed. The velocity/pressure coupling is solved with a pressure correction method [9], which consists in splitting the Navier-Stokes system into two stages, a velocity prediction and a pressure correction. The time interval $[0, T]$ is divided into $N$ equidistant time steps of length $\Delta t = T/N$. The approximate velocity and pressure fields at time $t^n = n\Delta t$, $(n = 0 \ldots N)$ are denoted $\mathbf{u}^n$ and $p^n$ respectively. Assuming all quantities are known up to $t^n$, the solution at $t^{n+1}$ results from the velocity prediction step:

*Find* $\mathbf{u}_*^{n+1}$ *such that*:

$$\begin{aligned} \rho \left( \frac{\mathbf{u}_*^{n+1} - \mathbf{u}^n}{\Delta t} + \nabla \cdot \left( \mathbf{u}_*^{n+1} \otimes \mathbf{u}^n \right) - \mathbf{u}_*^{n+1} \nabla \cdot \mathbf{u}^n \right) &= -\nabla p^n \\ + \nabla \cdot (\mu + \mu_t) \left( \nabla \mathbf{u}_*^{n+1} + \nabla^t \mathbf{u}_*^{n+1} \right) & \end{aligned} \tag{5}$$

followed by the pressure correction step:
*Find* $\mathbf{u}^{n+1}$ *and* $\phi^{n+1}$ *such that*:

$$\rho \frac{\mathbf{u}^{n+1} - \mathbf{u}_*^{n+1}}{\Delta t} + \nabla \phi^{n+1} = \mathbf{0} \tag{6}$$

$$\nabla \cdot \mathbf{u}^{n+1} = 0 \tag{7}$$

with:

$$\phi^{n+1} = p^{n+1} - p^n. \tag{8}$$

Considering $\rho$ constant and taking the divergence of (6) gives:

$$\nabla \cdot \left( \frac{\Delta t}{\rho} \nabla \phi^{n+1} \right) = \nabla \cdot \mathbf{u}_*^{n+1}. \tag{9}$$

Once $\phi^{n+1}$ is computed, the divergence-free velocity and the pressure are obtained by:

$$\mathbf{u}^{n+1} = \mathbf{u}_*^{n+1} - \frac{\Delta t}{\rho} \nabla \phi^{n+1}, \tag{10}$$

$$p^{n+1} = \phi^{n+1} + p^n. \tag{11}$$

The space derivatives of the inertial term are discretized by a hybrid Upwind-Centered scheme [22] and the viscous term is approximated by a second order centered scheme. The interface tracking is achieved by a Volume Of Fluid method (VOF): i.e. a Lax-Wendroff TVD scheme (Total Variation Diminishing), which is able to handle interface reconnections without interface reconstruction, is used to solve directly the free-surface evolutions [16]. The MPI library is used to parallelize the code. The mesh is partitioned into equal size subdomains to ensure load balancing. Communications between processors are also minimized. The HYPRE parallel solver and preconditioner library is used to solve the linear systems [7]. The prediction and correction steps are solved, respectively, thanks to a BiCGStab solver, associated with a point Jacobi preconditioner, and a GMRES solver, associated with a multigrid preconditioner. The numerical code has already been extensively verified and validated through numerous test-cases including mesh refinement analysis [17,20]. The accuracy of the numerical schemes and the conservation laws of mass and energy in the computational domain have been accurately verified.

### 2.3 Subgrid-scale model

The Smagorinsky model is usually used in Large Eddy Simulations, but it has been proved to be much too dissipative [24]. In our study, the turbulent viscosity is calculated with the Mixed Scale model [24].

This model exhibits a triple dependency on the large and small structures of the resolved field as a function of the cut-off length, which makes this model much more efficient than The Smagorinsky model. The eddy viscosity $\mu_t$ is calculated as follows (Eq. 12):

$$\mu_t(\mathbf{x}, t) = \rho C_M \overline{\Delta}^{1+\alpha} \left( |\overline{S}| \right)^{\frac{\alpha}{2}} \left( q_c^2(\mathbf{x}, t) \right)^{\frac{1-\alpha}{2}} \tag{12}$$

where $\overline{S}$ is the resolved deformation rate tensor, $C_M$ is the model constant chosen as $C_M = 0.06$, $\alpha$ is a parameter which value varies between 0 and 1. Generally, and in the following, $\alpha$ is taken to be equal to 0.5. The cut-off length of the filter $\overline{\Delta}$ is evaluated as follows:

$$\overline{\Delta} = (\Delta x \Delta y \Delta z)^{\frac{1}{3}} \tag{13}$$

where $\Delta x$, $\Delta y$ and $\Delta z$ are the sizes of the mesh grids in the respective directions, and $x$, $y$ and $z$, respectively, are the longitudinal, lateral and horizontal coordinates. The quantity $q_c$ represents the kinetic energy of the test field extracted from the resolved velocity field through the application of a test filter associated to the cut-off lengthscale $\widetilde{\overline{\Delta}} > \overline{\Delta}$. We choose $\widetilde{\overline{\Delta}} = 2\overline{\Delta}$, because it is the value which is most used and seems to give the best results [24]. This subgrid kinetic energy is supposed to be equal to the kinetic energy at cut-off $q_c^2$, evaluated in real space as (Eq. 14):

$$q_c^2(\mathbf{x}, t) = \frac{1}{2}\mathbf{u}(\mathbf{x}, t)'\mathbf{u}(\mathbf{x}, t)' \tag{14}$$

where the *test field* velocity ($\mathbf{u}'$) can be evaluated thanks to an explicit *test filter* applied to the resolved scales, noted ($\widetilde{\cdot}$) (Eq. 15):

$$(\mathbf{u}') = \mathbf{u} - \widetilde{\mathbf{u}} \tag{15}$$

This explicit discrete filtering operation is a linear combination of the neighboring values [24,25]. A three-dimensional test filter results from the tensorial product of the following mono-dimensional three-points filter (Eq. 16):

$$\widetilde{\overline{f_i}} = \frac{1}{6}\left(\overline{f}_{i+1} + 4\overline{f_i} + \overline{f}_{i-1}\right) \tag{16}$$

This weighted average is obtained by applying the Simpson rule to compute the average of the resolved variable $\overline{f}$ over the control cell surrounding the $i$th point. This test field velocity represents the high frequency part of the resolved velocity field. The use of this model does not require any complementary wall model, as the Smagorinsky model does, because the eddy viscosity vanishes when the kinetic energy tends to zero at cut-off.

### 2.4 Validation: a solitary wave colliding a vertical end-wall

Solitary waves are known for having some interesting properties: indeed, such a wave has a symmetrical form with a single hump and propagates with a uniform velocity without changing form. The solitary wave is completely defined for a given depth of water, $d$, and a dimensional amplitude $H$. Interactions occurring between solitary waves are of major interest, especially the direct, head-on collision between two waves traveling in opposite directions [17,19]. Maxworthy [21] experimented head-on colliding waves and showed that the waves reach maximum amplitudes greater than the sum of the initial wave amplitudes. The reflexion occurring when a single wave hits a vertical end-wall was also considered. Su and Mirie [27] developed analytical solutions for calculating the effects of the head-on collision, up to the third order of accuracy. The waves emerging from the collision have been shown to preserve their original identities to the third-order of accuracy. The maximum run-up amplitude reached during the collision of the two solitary waves has also been analytically calculated, as a function of both propagating wave amplitudes.

The subscripts $R$ and $L$ refers to the right- and left-going waves, respectively, heading towards each other. $\epsilon = H/d$ is the relative amplitude of the solitary wave. For two head-on colliding solitary waves with their maximum relative heights defined as $\epsilon_R$ and $\epsilon_L$, the maximum run-up $\eta_m$ is defined by:

$$\frac{\eta_m}{d} = \epsilon_R + \epsilon_L + \frac{\epsilon_R\epsilon_L}{2} + \frac{3}{8}\epsilon_R\epsilon_L(\epsilon_R + \epsilon_L) \tag{17}$$

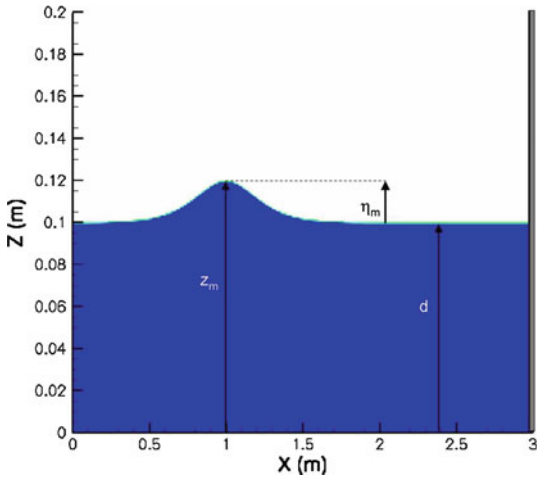


**Fig. 2** Initial conditions for the solitary wave end-wall collision test-case. $t = 0$ s, $\epsilon = 0.2$, $C > 0.5$

If we consider two identical solitary waves $\epsilon_R = \epsilon_L = \epsilon$, then:

$$\frac{\eta_m}{d} = 2\epsilon + \frac{\epsilon^2}{2} + \frac{3}{4}\epsilon^3 \tag{18}$$

Since the system of two head-on colliding waves of equal amplitude is symmetric about the mid-plane, it can be modelled by a single wave hitting a vertical end-wall [21]. Thus, the solution (18) can be used to show the ability of the numerical tool to reproduce accurately the impact and run-up of a wave on a vertical end-wall. First-order solitary wave theory is used for the initial wave shape and wave velocity [17,18].

A systematical study is proposed, the water depth being $d = 0.1$ m, the amplitudes varying from $\epsilon = 0.1$ to $\epsilon = 0.6$. The crests are located at $x_{crest} = 1$ m at the beginning of the calculation. All calculations are made with the densities and the viscosities of air and water. The numerical domain is 3 m long and 0.2 m high. It is discretized into $600 \times 200$ regular Cartesian grids. A no-slip condition was imposed at the lower boundary and an open boundary condition is used at the top of the numerical domain. We illustrate hereafter (Figs. 2, 3, 4) the different steps of the collision for the case $\epsilon = 0.2$, which gives a dimensional amplitude $\eta = 0.02$ m and a maximum waveheight $z = 0.12$ m. The initial wave celerity is $c = 1.085\,\mathrm{m\,s^{-1}}$. We can see the wave propagating towards the right boundary of the domain (Fig. 4a–c) to reach its maximum run-up $z_m = 0.14058$ m ($\eta_m/d = 0.4058$) (Fig. 3) at $t = 1.80$ s, to be compared with the predicted value $z_m = 0.140206$ m ($\eta_m/d = 0.40206$) (which gives an error of 0.3%).

We show hereafter (Fig. 5) the plot of our numerical results compared to those found in literature. We could then observe a very good agreement between our numerical results and those, experimental, numerical and analytical, compiled in [27]. The general trend is followed with a reasonable accuracy. The discrepancies come from the fact that the analytical developments from [27] were performed for head-on colliding waves, without taking into account the friction effects when waves interact with walls. It agrees very well anyway with the published results of wave-wall reflexions [1,21].

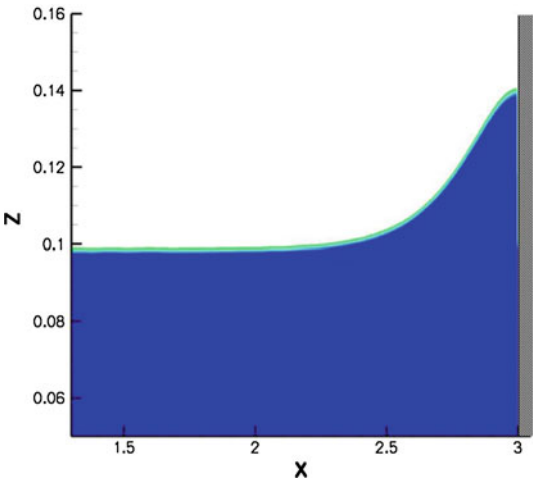


**Fig. 3** Maximum run-up for the collision at $t = 1.80\,\mathrm{s}$. $\epsilon = 0.2$, $C > 0.5$

## 3 Numerical modelling of a breaking tidal bore

The experimental configuration is the generation of a weak positive surge by a rapid partial gate closure at the downstream end of the control volume and its upstream propagation against the initially steady flow [13,15].

### 3.1 Presentation of the case study

The numerical configuration consists in an initial rectangular steady flow motion (from the right side of the numerical domain to the left side) with an initial steady velocity ($V_0 = 1.021\,\mathrm{m\,s^{-1}}$), impacting a wall boundary located at the left side of the numerical domain. When the initial rectangle of water hits the wall, the water runs-up the wall and splashes down. A breaking bore is then generated and propagates upstream, towards the right side of the numerical domain. The numerical tool has been shown to model accurately the impact and run-up of a wave on a vertical wall in Sect. 2.4.

The two-dimensional numerical domain is 10 m long and 1 m high. The initial water depth is $d_0 = 0.0785\,\mathrm{m}$, as presented in Fig. 6. A no-slip condition was imposed at the lower boundary and an open boundary condition is used at the top of the numerical domain. At the left side of the numerical domain, an outlet velocity condition ($V_{out} \simeq 1.76\,\mathrm{m\,s^{-1}}$) is fixed to let the water flow below a vertical gate, the outlet height being $h_{out} = 0.02\,\mathrm{m}$. The inlet velocity ($V_{in} = 1.021\,\mathrm{m\,s^{-1}}$) is fixed at the right side of the numerical domain at the inlet height $h_{in} = d_0 = 0.0785\,\mathrm{m}$. The time step is chosen to ensure a Courant-Friedrichs-Levy number less than 0.1. The calculation is made with the densities and the viscosities of air and water ($\rho_a = 1.1768\,\mathrm{kg\,m^{-3}}$ and $\rho_w = 1000\,\mathrm{kg\,m^{-3}}$, $\mu_a = 1.85 \times 10^{-5}\,\mathrm{kg\,m^{-1}\,s^{-1}}$ and $\mu_w = 1 \times 10^{-3}\mathrm{kg\,m^{-1}\,s^{-1}}$). Hydrostatic pressure is initialized in the rectangle of water. The numerical domain, discretized into $2000 \times 1000$ regular Cartesian cells, is partitioned into 128 subdomains (one processor per subdomain). The Froude number is $Fr = 1.77$.

In the next sections, some large structures will be observed and described: a main recirculation structure observed beneath the bore front and propagating upstream (towards the right side of the numerical domain), and some macroturbulent structures separating for the previous one and propagating downstream (towards the left side of the numerical domain).

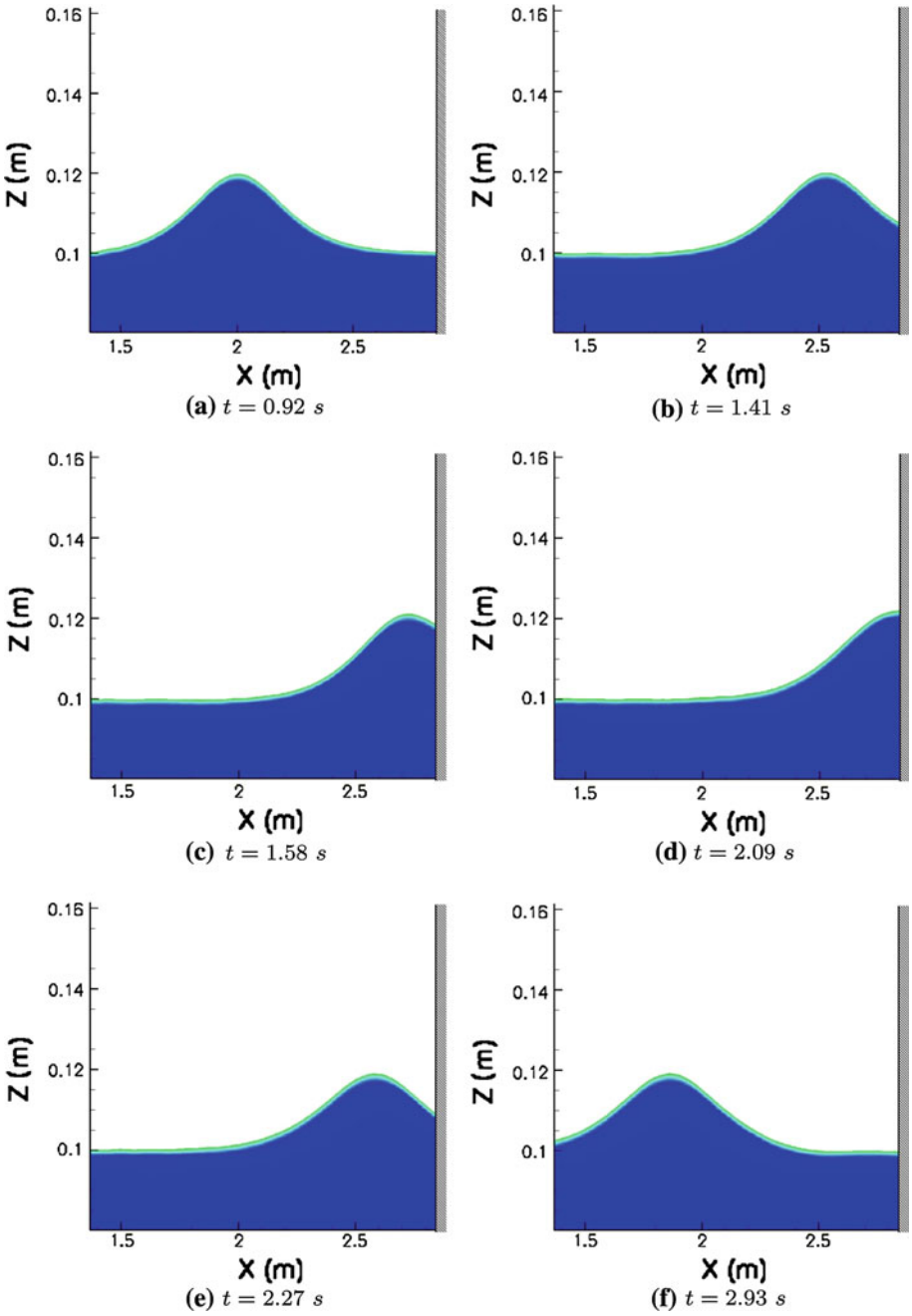


**Fig. 4** Details of the end-wall collision at various instants. $\epsilon = 0.2$, $C > 0.5$. From (**a**) to (**c**), the solitary wave is propagating towards the wall—from (**d**) to (**f**), the solitary wave is propagating towards the left side of the numerical domain

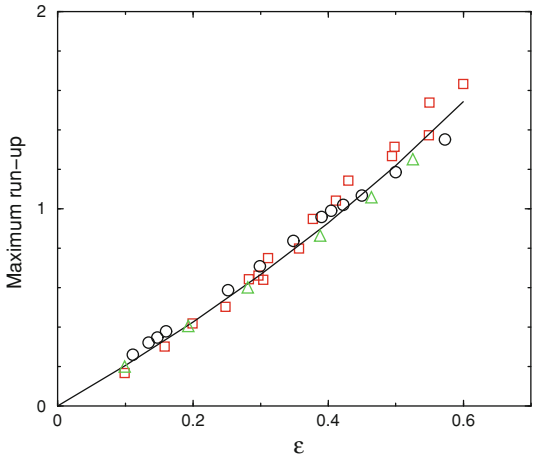


**Fig. 5** Maximum wave run-up, $\eta_m/d$, plotted versus wave non-dimensional amplitude, $\epsilon$. *Black line*: 3rd order analytical results from [27] (Eq. 18); *black circle*: experimental results from [21]; *red square*: numerical results from [1]; *green triangle*: present numerical results

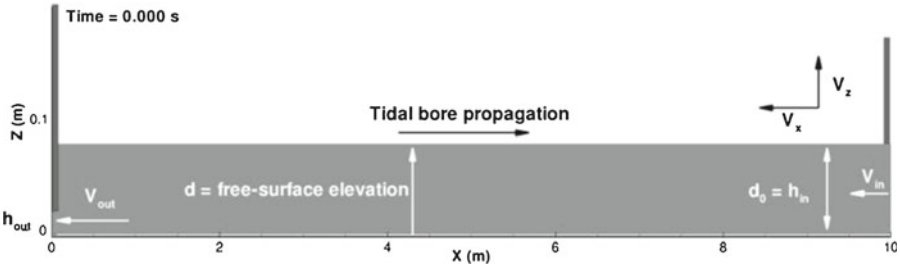


**Fig. 6** Sketch of the initial conditions for the tidal bore generation, immediately after the gate closure corresponding to the wall boundary condition set at the left side of the numerical domain

The structures are generated in sequence, the continuous process of generation exhibiting some regular temporal and spatial frequencies.

### 3.2 Results

Figure 7 shows the initial rectangle of water impacting the left, downstream wall, the water running-up the wall and splashing down. The bore then propagates towards the right, upstream side of the numerical domain. Some air entrainment is detailed and large structures are observed under the bore front. The generated bore then propagates upstream towards the right side of the numerical domain. The initial large free-surface deformations are in agreement with the experimental photographs and movies [13]. The celerity of the bore front is approximatively $0.5\,\mathrm{m\,s^{-1}}$, that is close to the experimental value of $0.54\,\mathrm{m\,s^{-1}}$ recorded at $x = 5\,\mathrm{m}$. The velocity field, presented in air and water, illustrates the strong agitation generated in the air by the bore generation.

Figure 8 shows the free-surface profile plotted against the dimensionless time. Figure 9 presents the dimensionless horizontal and vertical velocity components, $V_x/V_*$ and $V_z/V_*$ respectively, as functions of the dimensionless time. All presented profiles have been checked to be established at various longitudinal locations. $V_*$ is the shear velocity, experimentally measured $V_* = 0.044\,\mathrm{m\,s^{-1}}$ [13]. The horizontal velocity $V_x$ is positive in the downstream direction: i.e., from right to left. The bore front passage is associated with a rapid flow

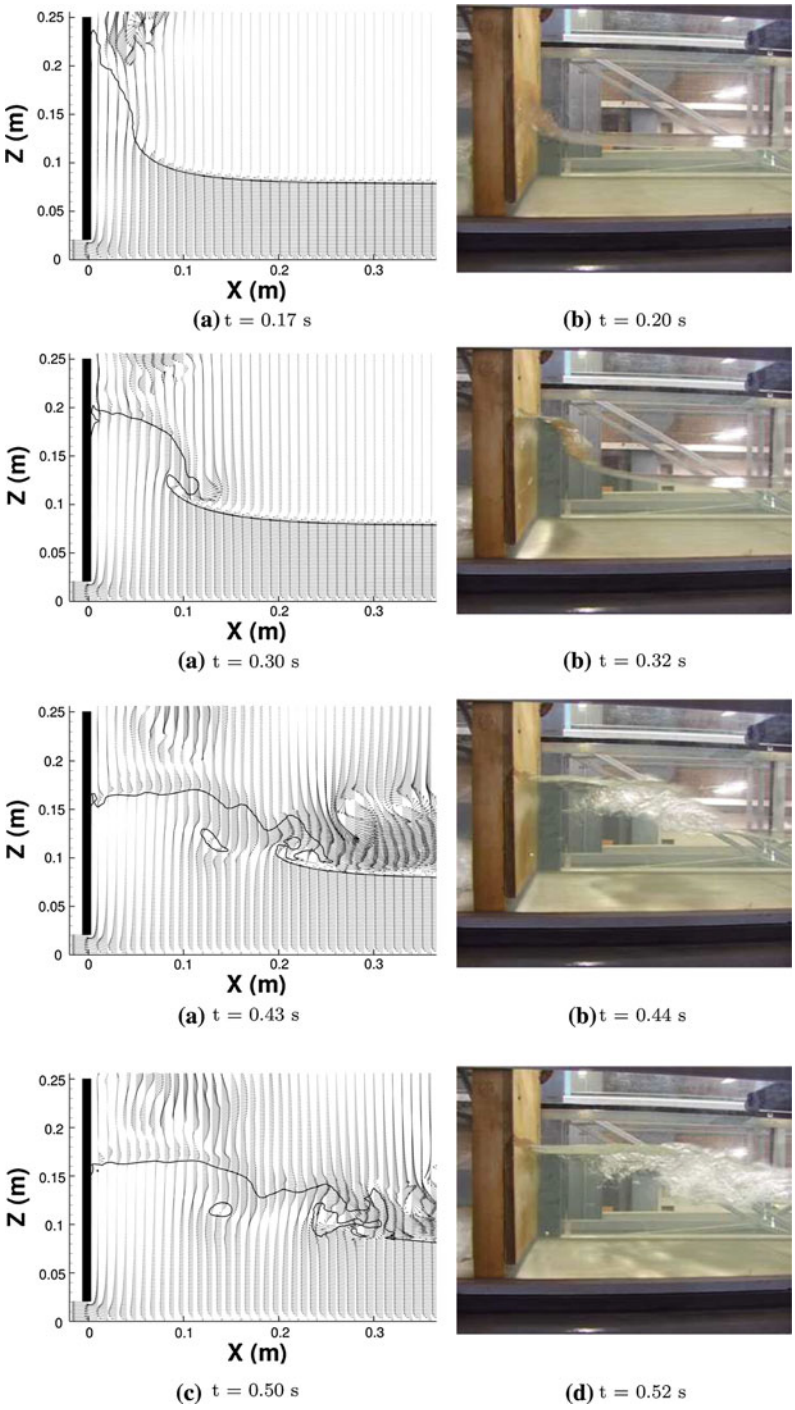


**Fig. 7** Initial impact on the left wall and bore generation. *Left column*: numerical results—only one vector over two is shown in air and water. *Right column*: experimental photographs of the bore generation

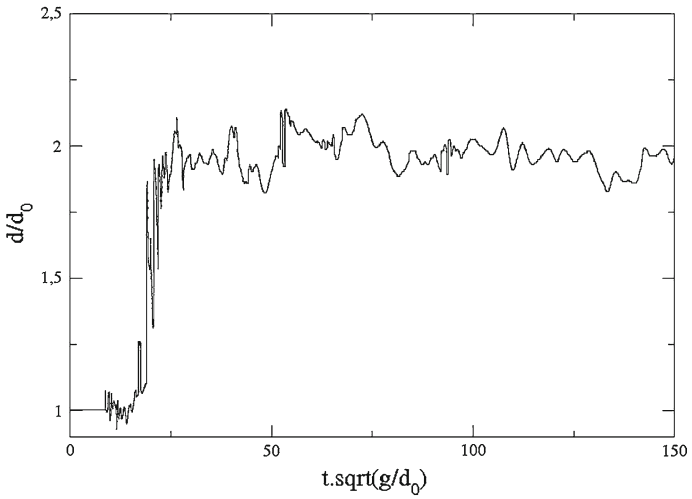


**Fig. 8** Dimensionless instantaneous water depth $d/d_0$ as function of dimensionless time at $x = 1$ m from the gate

deceleration, coupled with a sudden increase in water depth. The numerical data are close of the physical data [13,15] and qualitatively in agreement with some field data [26]. Some flow reversal (negative values of streamwise velocity) is observed next to the bed ($z/d_0 \leq 0.2$ in Fig. 9), while this feature is absent from $z/d_0 = 0.3$. This pattern is associated with some transient flow separation and recirculation [13,15]. It can also be noted that, next to the bed, the largest vertical velocity magnitudes are observed when the bore front is passing. Moreover, larger vertical velocity variations are present in the upper part of the water column, associated with air entrainment, splashes, free-surface fluctuations and vortical structures present in the roller.

Some air entrainment occurs near the free-surface in the bore roller and some large recirculation structures are observed beneath the bore front, as shown in Fig. 10. The air bubble entrainment is a well-known feature of breaking tidal bores that is observed in laboratory [13,15] and in the field (Fig. 1c). It is believed to be a main source to the tidal bore rumble noise [5]. The large vortical structures (Fig. 10) remain next to the bed as these persisting coherent structures are advected towards the left side of the numerical domain while the breaking bore propagates upstream, towards the right side of the numerical domain. The height of these large eddies can reach up to approximately half of the downstream water depth, at the time of their generation.

A video is available in a digital appendix (Online Resource 1 in Supplementary material). The propagation of the weak breaking bore is shown between $x = 6$ m and $x = 7$ m, during 4.732 s (from $t = 10.257$ s to $t = 14.989$ s), when it has reached a constant celerity. The streamlines are animated with the free-surface to clearly illustrate the recirculation structures generation. The streamlines are first parallel to the bottom, as the water flows downstream (towards the left side of the movie window). Then, the streamlines rise, indicating the bore front arrival at the left, downstream side of the window movie, and the main large flat-shaped recirculation cell appears. It then grows in size as the water depth suddenly increases. At $t \backsimeq 10.8$ s, this cell splits in a smaller structure. The main large flat-shaped cell keeps propagating upstream as the recirculation structure separates at $t \backsimeq 10.9$ s and is released to propagate downstream. At $t \backsimeq 11$ s, the main cell is splitting again to generate

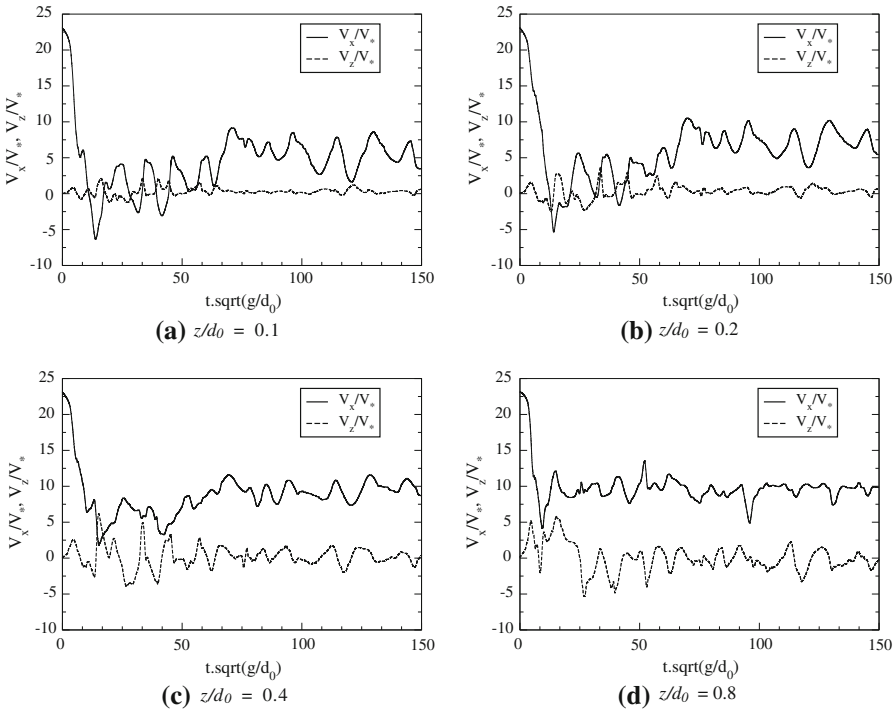


**Fig. 9** Dimensionless velocity components as functions of dimensionless time beneath the tidal bore

another macroturbulent structure. This process repeats itself regularly in time. The eddies are spaced every 20 cm from each other, as illustrated in Fig. 10. At $t \backsimeq 12.72$ s (Fig. 10a), a structure is about to leave the picture frame at the left side, while another structure is about to be released in the main flow. The three structures are observed to be preceded by the main flat-shaped cell propagating upstream under the bore front. At $t \backsimeq 14.45$ s (Fig. 10b), an eddy is advected downstream by the main flow. It is followed by another structure shed by the main cell. An acceleration is observed when the structures separate and go downstream, as they were attached to the main cell propagating upstream. At the right side of the pictures, two other structures can be clearly identified, as they are separating one after the other.

The eddies are advected downstream at about $V_{adv} \simeq 0.3\,\mathrm{m\,s^{-1}}$, which gives a ratio $V_{adv}/V_2 \simeq 0.6$, where $V_2$ is the flow velocity after the bore passage. Once the eddies start propagating downstream, their size slowly decreases. The dimensionless Strouhal number of the process is $St = \dfrac{f d_2}{V_2} \simeq 1.42$, with $f$ the frequency of vortex shedding and $d_2 \simeq 0.16$ m is the water depth after the bore passage.

Figure 11 illustrates the instantaneous pressure distributions under the breaking tidal bore. The pressure levels are distorted by the presence of the eddies, the cores of the rotating structures being associated with low pressure levels.

### 3.3 Discussion

Both physical and numerical data suggest some energetic turbulent events beneath and after the tidal bore front (Figs. 10, 11). The structures are generated in sequence below the bore

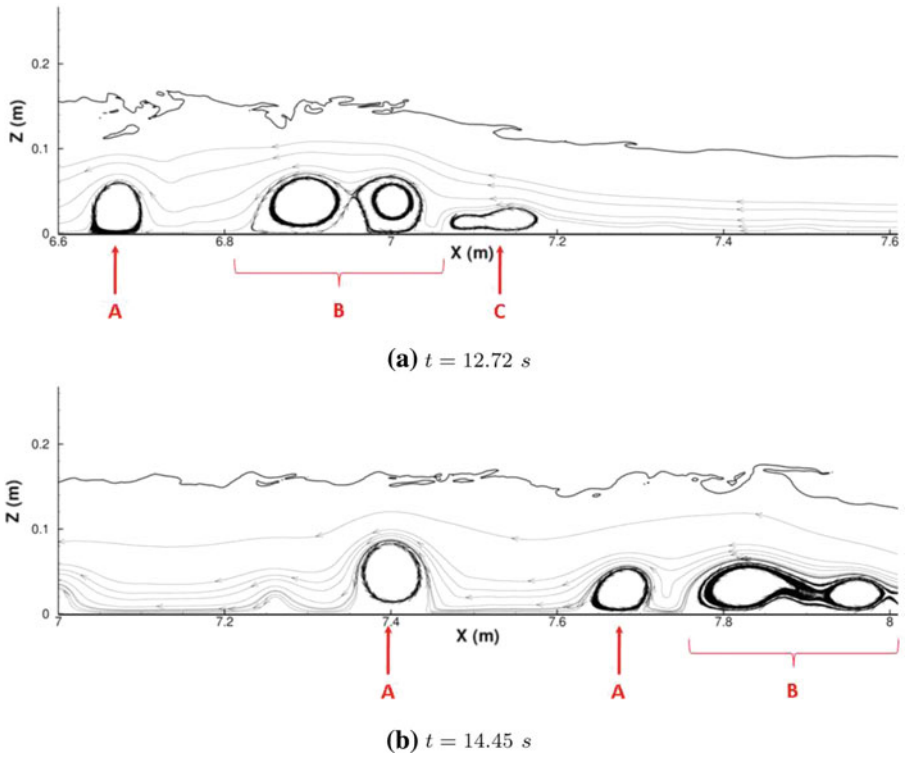


**Fig. 10** Streamlines indicating recirculation structures under the propagating tidal bore (propagation from *left to right*). Macroturbulent structures propagate downstream (*A*), separating structures (*B*), shedding and propagating downstream, main recirculation structure propagates upstream (*C*)

front, the continuous process exhibiting some regular temporal and spatial frequencies. The numerical modelling data show some large vertical velocity variations implying the generation of vorticity behind the bore front. These large-scale vortical structures remain near the bed as the bore propagates upstream and the presence of these persisting, coherent structures implies that a great amount of sediment could be placed into suspension and transported by the main flow. These original results confirm and illustrate the experimental observations identifying for the first time these recirculations under tidal bores [13,15].

The preliminary numerical results are limited by two aspects. First, the numerical configuration is two-dimensional. Second, there is a need for some realistic unsteady inflow conditions to be specified at the inlet boundary. Some numerical simulations were tested by generating turbulent inflow data consisting of the time-averaged experimental velocity profile with some superimposed random fluctuations. The generated data do not exhibit any spatial or temporal correlations, and the pseudo turbulence is quickly dissipated. An effective method to generate synthetic eddies on the inlet plane is under implementation [11].

## 4 Conclusion and future work

A Large Eddy Simulation (LES) was performed to investigate the turbulent flow motion of a breaking tidal bore in a two-dimensional configuration. The major result of this ongoing

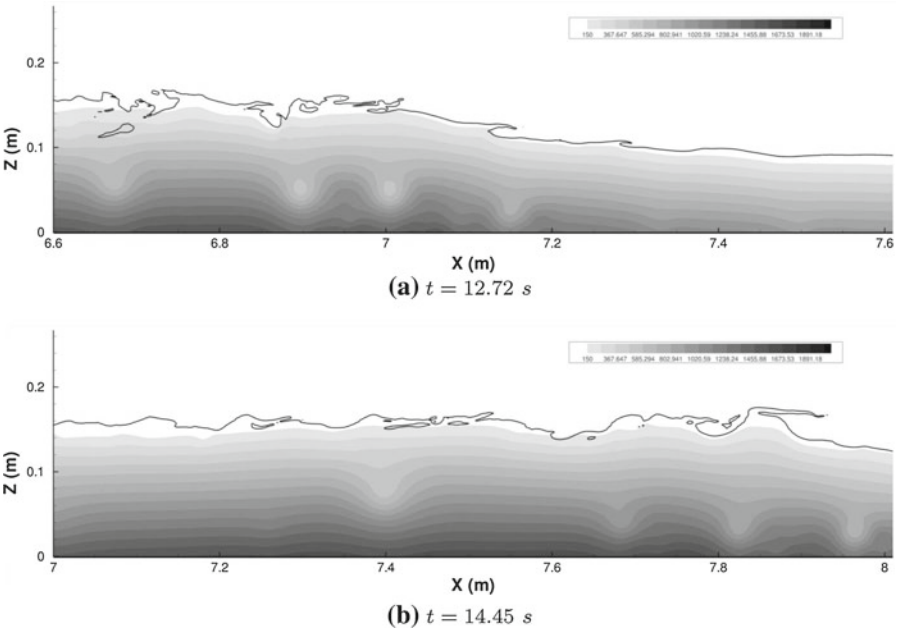


**Fig. 11** Pressure levels indicating recirculation structures under the propagating tidal bore (propagation from *left to right*)

work is the identification of recirculation structures generated in sequence below the front of the propagating tidal bore and advected downstream. The main features of the flow are in accordance with the basic experimental results (weak breaking bore, flow reversal and rapid flow deceleration). A breaking bore with a formed roller was studied specifically. The arrival of the bore roller was marked by a discontinuity of the water depth associated with a sudden longitudinal deceleration. Some interesting features were highlighted, including some transient recirculation structures that must be responsible for some bed erosion and vertical mixing of the water column when a tidal bore propagates upstream in the estuarine zone of a natural river. Some large velocity fluctuations of horizontal and vertical velocity components were observed also during the tidal bore front passage in beneath the following waves (called whelps). The numerical results were found to be in good accordance with experimental data. In the future, the undular tidal bore should also be studied and the physical processes should be compared.

Some 3D numerical developments are undertaken to overcome the limitations of the inlet boundary conditions, to confirm these first observations and to investigate more into details the generation process of the recirculation structures and their three dimensional features. Definitely, any numerical simulation of a natural system does require a 3D simulation technique.

**Acknowledgements** The authors wish to thank the Aquitaine Regional Council for the financial support dedicated to a 256-processor cluster investment, located in the TREFLE laboratory. This work was granted access to the HPC resources of CINES under the allocation 2009-c2009026104 made by Grand Equipement National de Calcul Intensif (GENCI). Prof. Hubert Chanson also acknowledges the funding for a visiting professorship position at the Université de Bordeaux and a fellowship from the Australian Academy of Science.

## References


1. Chan RKC, Street RL (1970) A computer study of finite amplitude water waves. J Comput Phys 6: 68–94
2. Chanson H (2005) Physical modelling of the flow field in an undular tidal bore. J Hydraul Res 43: 234–244
3. Chanson H (2008) Turbulence in positive surges and tidal bores—effects of bed roughness and adverse bed slopes. Technical report no. CH68/08. Department of Civil Engineering, The University of Queensland, Brisbane, Australia
4. Chanson H (2009) Current knowledge in hydraulic jumps and related phenomena. A survey of experimental results. Eur J Mech B 28(2):191–210
5. Chanson H (2009) The rumble sound generated by a tidal bore event in the baie du mont saint michel. J Acoust Soc Am 125(6):3561–3568
6. Donnelly C, Chanson H (2005) Environmental impact of undular tidal bores in tropical rivers. Environ Fluid Mech 5:481–494
7. Falgout RD, Jones JE, Yang UM (2006) The design and implementation of *hypre*, a library of parallel high performance preconditioners, Chap 51. In: Bruaset AM, Tveito A (eds) Numerical solution of partial differential equations on parallel computers. Springer-Verlag, New York, pp 267–294
8. Furuyama SI, Chanson H (2008) A numerical study of open channel flow hydrodynamics and turbulence of the tidal bore and dam-break flows. Technical report no. CH66/08. Division of Civil Engineering, The University of Queensland, Brisbane, Australia
9. Goda K (1978) A multistep technique with implicit difference schemes for calculating two- or three-dimensional cavity flows. J Comput Phys 30:76–95
10. Helluy P, Gollay F, Grilli ST, Seguin N, Lubin P, Caltagirone JP, Vincent S, Drevard D, Marcer R (2005) Numerical simulations of wave breaking. Math Model Numer Anal 39(3):591–608
11. Jarrin N, Benhamadouche S, Laurence D, Prosser R (2006) A synthetic-eddy-method for generating inflow conditions for large-eddy simulations. Int J Heat Fluid Flow 27:585–593
12. Kataoka I (1986) Local instant formulation of two-phase flow. Int J Multiph Flow 12(5):745–758
13. Koch C, Chanson H (2005) An experimental study of tidal bores and positive surges: hydrodynamics and turbulence of the bore front. Technical report no. CH56/05. Department of Civil Engineering, The University of Queensland, Brisbane, Australia
14. Koch C, Chanson H (2008) Turbulent mixing beneath an undular bore front. J Coast Res 24:999–1007
15. Koch C, Chanson H (2009) Turbulence measurements in positive surges and bores. J Hydraul Res 47(1):29–40
16. LeVeque RJ (1992) Numerical methods for conservation laws. Lectures in mathematics. Birkhauser, Zurich
17. Lubin P (2004) Large eddy simulation of plunging breaking waves. PhD thesis, Université Bordeaux I (in English)
18. Lubin P, Lemonnier H (2004) Propagation of solitary waves in constant depths over horizontal beds. Multiph Sci Technol 16(1–3):237–248
19. Lubin P, Vincent S, Caltagirone JP (2005) On the navier-stokes equations simulation of the head-on collision between two surface solitary waves. C R Mécanique 333(4):351–357
20. Lubin P, Vincent S, Abadie S, Caltagirone JP (2006) Three-dimensional large eddy simulation of air entrainment under plunging breaking waves. Coast Eng 53:631–655
21. Maxworthy T (1976) Experiments on collisions between solitary waves. J Fluid Mech 76:177–185
22. Patankar SV (1990) Numerical heat transfer and fluid flow. Hemisphere Publishing Corporation, New York
23. Rudman M (1998) A volume-tracking method for incompressible multifluid flows with large density variations. Int J Numer Meth Fluids 28(2):357–378
24. Sagaut P (1998) Large Eddy Simulation for incompressible flows—an introduction. Springer Verlag, Berlin
25. Sagaut P, Grohens R (1999) Discrete filters for large eddy simulation. Int J Numer Meth Fluids 31:1195–1220
26. Simpson JH, Fisher NR, Wiles P (2004) Reynolds stress and tke production in an estuary with a tidal bore. Estuar Coast Shelf Sci 60:619–627
27. Su CH, Mirie RM (1980) On head-on collision between two solitary waves. J Fluid Mech 98:509–525
28. Tessier B, Terwindt JHJ (1994) An example of soft sediment deformations in an intertidal environment: the effect of a tidal bore. Comptes Rendus—Academie des Sciences, Serie II 319:217–223
29. Wolanski E, Moore K, Spagnol S, D'Adamo N, Pattiaratchi C (2001) Rapid, human-induced siltation of the macro-tidal ord river estuary, western australia. Estuar Coast Shelf Sci 53:717–732

30. Wolanski E, Williams D, Spagnol S, Chanson H (2004) Undular tidal bore dynamics in the daly estuary, northern australia. Estuar Coast Shelf Sci 60:629–636
31. Wolanski E, Williams D, Hanert E (2006) The sediment trapping efficiency of the macro-tidal daly estuary, tropical australia. Estuar Coast Shelf Sci 69:291–298